

Operation of the CESR-TA vertical beam size monitor at $E_b=4$ GeV

J. P. Alexander^a, C. Conolly^a, E. Edwards^a, J. W. Flanagan^{b,c}, E. Fontes^a, B. K. Heltsley^{a,*}, A. Lyndaker^a, D. P. Peterson^a,
N. T. Rider^a, D. L. Rubin^a, R. Seeley^a, J. Shanks^a

^aCornell University, Ithaca, NY 14853, USA

^bHigh Energy Accelerator Research Organization (KEK), Tsukuba, Japan

^cDepartment of Accelerator Science, Graduate University for Advanced Studies (SOKENDAI), Tsukuba, Japan

Abstract

We describe operation of the CESR-TA vertical beam size monitor (xBSM) with e^\pm beams with $E_b=4$ GeV. The xBSM measures vertical beam size by imaging synchrotron radiation x-rays through an optical element onto a detector array of 32 InGaAs photodiodes with 50 μm pitch. The device has previously been successfully used to measure vertical beam sizes of 10 – 100 μm on a bunch-by-bunch, turn-by-turn basis at e^\pm beam energies of ~ 2 GeV and source magnetic fields below 2.8 kG, for which the detector required calibration for incident x-rays of 1-5 keV. At $E_b = 4.0$ GeV and $B=4.5$ kG, however, the incident synchrotron radiation spectrum extends to ~ 20 keV, requiring calibration of detector response in that regime. Such a calibration is described and then used to analyze data taken with several different thicknesses of filters in front of the detector. We obtain a relative precision of better than 4% on beam size measurement from 15-100 μm over several different ranges of x-ray energy, including both 1-12 keV and 6-17 keV. The response of an identical detector, but tilted vertically by 60° in order to increase magnification without a longer beamline, is measured and shown to improve x-ray detection above 4 keV without compromising sensitivity to beam size. We also investigate operation of a coded aperture using gold masking backed by synthetic diamond.

Keywords: electron beam size, x-ray diffraction, pinhole, coded aperture, synchrotron radiation, electron storage ring

1. Introduction

The CESR-TA x-ray beam size monitor [1, 2] (xBSM) images synchrotron radiation from a hard-bend magnet through a single- or multi-slit optical element onto a 32-strip photodiode detector [3] with 50 μm pitch and sub-ns response. A simplified schematic of the CESR-TA xBSM setup is shown in Fig. 1, and dimensions appear in Table 1. Separate installations exist for electrons and positrons. The hard-bend magnets have a bending radius of 31.1 m. The vertical beam size σ_b is extracted from a fit of the image for each bunch and turn to a set of unit-area templates; each template has convolved the point response function (prf) with Gaussian smearing for a particular beam size and magnification. Each such fit also yields a vertical beam position y_b and amplitude A_b . Ref. [1] describes our use of both single-slit (pinhole) and multi-slit optical elements, the latter of which are known as coded apertures, for e^\pm beam energies of $E_b=1.8$ -2.6 GeV. In order to accurately predict the point response functions, in [1] we determined the detector's spectral response to x-rays up to about 5 keV. In [2], we gave a detailed description of the design and operation of two silicon-backed coded apertures.

Extending characterization of our detector's spectral response above 5 keV is useful for two reasons. First, a similar detector is an option for beam size measurement using x-rays from the SuperKEKB positron ($E_b=4$ GeV) and electron

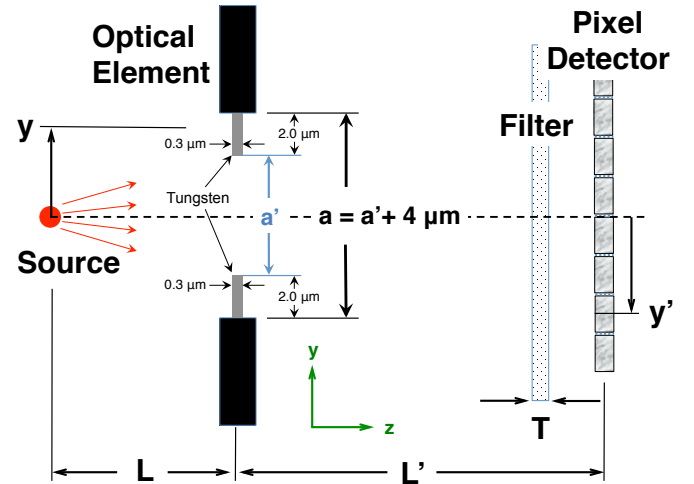


Figure 1: Simplified schematic of xBSM layout (not to scale), shown with a model of the adjustable pinhole (PH) optical element. Dimensions appear in Table 1.

($E_b=7$ GeV) beams. Second, a new, dedicated xBSM installation at CESR is being designed. Unlike the current setup, it will be able to operate in both CESR-TA (beam energies of ~ 2 GeV) and CHESS ($E_b=5.3$ -6.5 GeV) operating conditions. In both scenarios a substantial fraction of the x-ray spectrum will be above 5 keV, as is evident in Fig. 3 when comparing existing ($B<4.5$ kG) and planned ($B=4.5$ kG) installations. In Fig. 2, the response as determined in [1] is shown; note that the data acquired for $E_b=1.8$ -2.6 GeV could not distinguish between the

*Corresponding author

Email address: bkh2@cornell.edu (B. K. Heltsley)

Table 1: Geometrical parameters defining the CESR-TA xBSM beamlines. Geometrical quantities are defined in Fig. 1. Distances assume the coded aperture optic; the pinhole optic is 25 mm closer to the source point and hence has a magnification value about 1% larger than shown. The uncertainties on L are from an optical survey. The uncertainties on L' are from the survey, CESR orbit, and the associated depth of field.

Parameter	e^- beamline	e^+ beamline
L	4356.5 ± 3.9 mm	4485.2 ± 4.0 mm
L'	10621.1 ± 1.0 mm	10011.7 ± 1.0 mm
$M \equiv L'/L$	2.4380 ± 0.0022	2.2322 ± 0.0020
a'	$\approx 50 - 300$ μm	same as e^-
a	$\approx 50 - 1000$ μm	same as e^-
$2\theta_{\text{max}} = a'/L$	$11 - 69$ μrad	$11 - 67$ μrad

possible response shown as curve #1 from that of curve #3.

The balance of this paper is organized as follows. First, in Sect. 2, the opening in the adjustable pinhole optical element for data acquired at $E_b=4.0$ GeV is determined using techniques similar to those used in [1] for operation near $E_b=2$ GeV. Second, Sect. 3 describes measurement of the detector spectral response using $E_b=4.0$ GeV data, again using techniques previously described [1]. Third, in Sect. 4 we describe beam size measurements using several different x-ray ranges and a large range of beam sizes. Fourth, Sect. 5 reports on operation and calibration of the detector after tilting it vertically by 60° with respect to the incident x-rays. Finally, Sect. 6 describes evaluation of a prototype for a diamond-backed coded aperture for use at SuperKEKB, and Sect. 7 summarizes our conclusions.

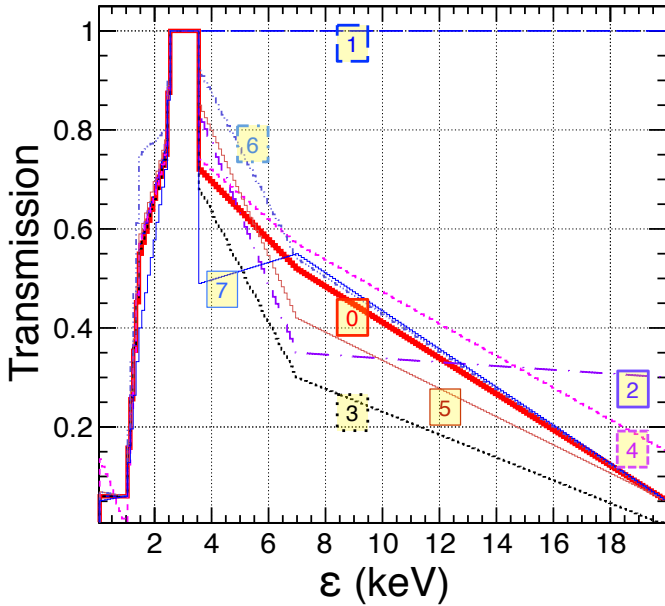


Figure 2: Spectral response curves used to explore sensitivity of measured beam size to the detected x-ray spectrum. The thickest solid curve represents the nominal spectrum and is labeled as “0”; seven other alternative responses consistent with the data of [1] are also shown and labeled with numbers from 1-7.

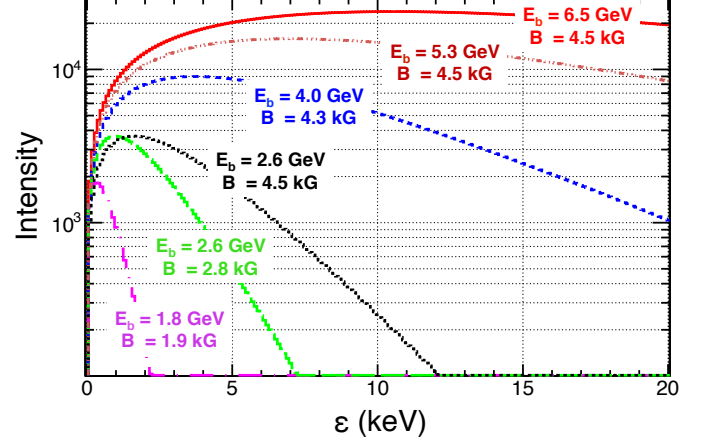


Figure 3: Spectra of x-rays for several e^\pm beam energy/magnetic field combinations, including a relative factor of ρ/γ (bend radius/ (E_b/m_e)) to account for source length due to the $1/\gamma$ horizontal width of the synchrotron radiation searchlight. The curves labeled with magnetic fields below 4.5 kG correspond to the current xBSM configuration; the 4.5 kG curves correspond to a planned upgrade with a dedicated, fixed-field source magnet.

2. Size of pinhole opening

To determine the size of the gap in the adjustable pinhole (PH) used for our filter studies at $E_b=4$ GeV, we follow a procedure similar to that described in Sect. 5.3 of Ref. [1], and apply it to $E_b=4$ GeV data and the corresponding predicted synchrotron radiation spectrum. We need to determine, for the PH model shown in Fig. 1, gap size a' used for data acquired at $E_b=4$ GeV. We know the motor setting ($mset = 4.22$), but need to determine its calibration to absolute distance.

The first step is to find the opening a' our model predicts to result in the narrowest prf for an incident x-ray spectrum for magnet field strength $B=0.43$ T (which preserves the required bending radius at $E_b=4.0$ GeV). Each point in Fig. 4 corresponds to the beam size reconstructed from the same 1024-turn run using a prf made with a different value of a' . The narrowest prf corresponds to the largest reconstructed beam size at

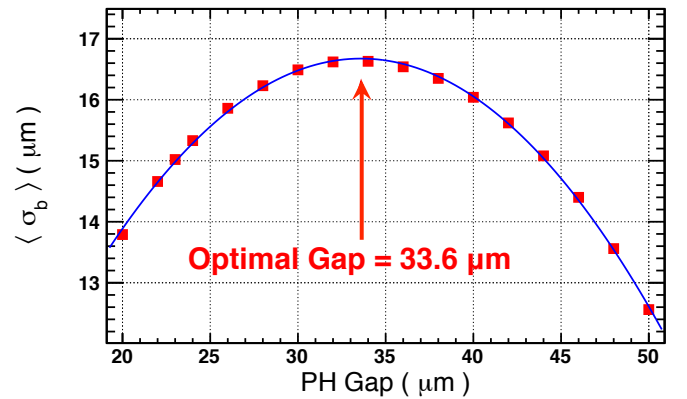


Figure 4: Turn-averaged beam size $\langle \sigma_b \rangle$ for the same run at $E_b=4.0$ GeV based on prf's using the specified value of a' with a parabolic fit to the points superimposed.

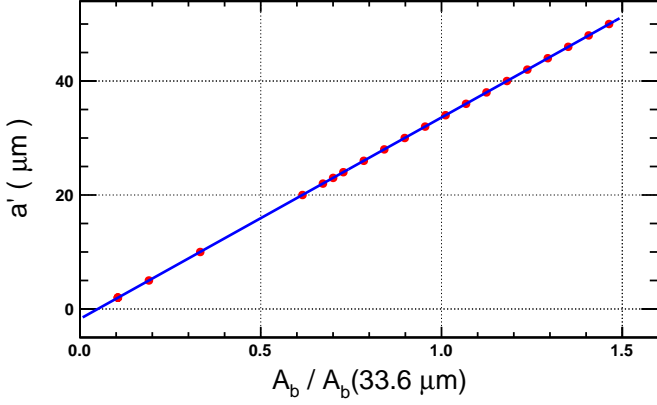


Figure 5: Model prediction for the pinhole gap opening a' vs. image amplitude A_b (relative to the value at $a'=33.6 \mu\text{m}$), with a linear fit to the points superimposed, all at $E_b=4.0 \text{ GeV}$.

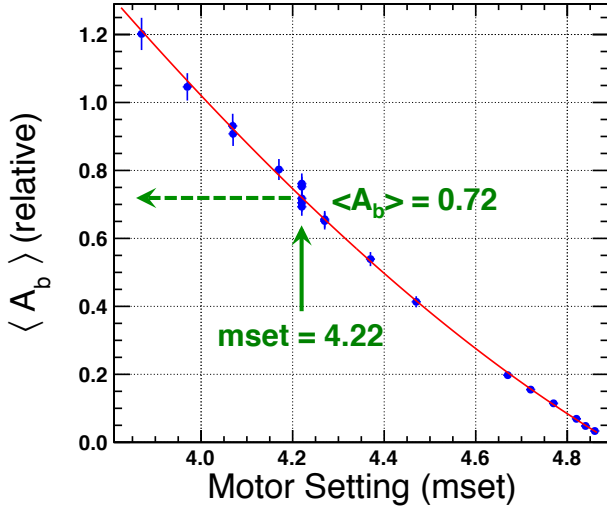


Figure 6: Relative turn-averaged image amplitude $\langle A_b \rangle$ vs. motor setting, $mset$, from the xBSM dataset taken at $E_b=4.0 \text{ GeV}$. The overlaid curve represents a second-order polynomial fit to the data points.

$a'=33.6 \mu\text{m}$. This becomes the reference value for amplitude.¹

The second step is to determine the formula relating relative image amplitude to the opening a' . Fig. 5 is generated from the expected x-ray spectrum, assumed spectral response, and the PH model, resulting in²

$$a'(\mu\text{m}) = 35.3 \times \frac{A_b}{A_b(a' = 33.6 \mu\text{m})} - 1.7. \quad (1)$$

What remains is to determine the relative area of images for the actual opening we used relative to the optimal value, $a'=33.6 \mu\text{m}$. In order to do so, several data runs were acquired

¹For this analysis, a measured value of “amplitude” represent the factor, divided by the bunch current in mA independently measured for that run, multiplying a unit-area template so as to yield a best-fit to the image data points.

²The formula in Eq. (1) has a non-zero offset due to the partially-transmitting “lips” at the two edges of the gap as shown in Fig. 1; i.e., some light is transmitted even for $a'=0$.

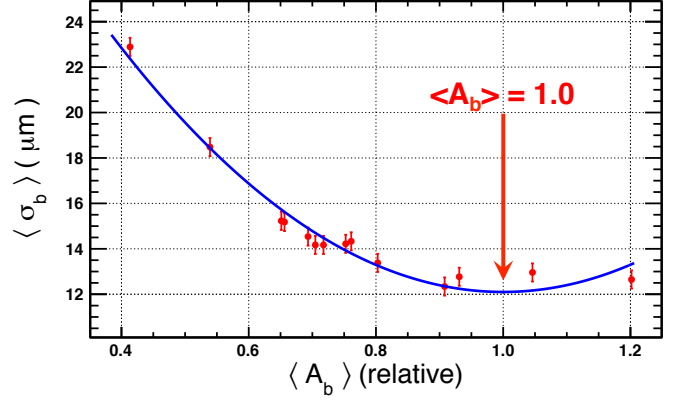


Figure 7: Turn-averaged beam size $\langle \sigma_b \rangle$ vs. relative turn-averaged image amplitude $\langle A_b \rangle$, from the xBSM dataset taken at $E_b=4.0 \text{ GeV}$. The overlaid curve represents a second-order polynomial fit to the data points.

with a variety of motor settings ($mset$) for the gap. The motor setting is known to be not quite linear with PH opening; this is apparent in Fig. 6 where the image amplitude is plotted vs. $mset$. The normalization for image amplitude comes from this same dataset, which can be seen in Fig. 7 to attain the narrowest image (by definition) at relative image size of 1.0. Using Eq. (1), the pinhole size, as extracted from $E_b=4.0 \text{ GeV}$ data, is $a' = 0.72 \times 35.3 - 1.7 = 23.7 \mu\text{m}$, with an estimated uncertainty of $1.0 \mu\text{m}$.

An independent dataset was acquired at $E_b=2.1 \text{ GeV}$ for a similar purpose. At this energy, the optimal $a'=50 \mu\text{m}$ [1] and Eq. (19) from Ref. [1] applies. Figs. 8 and 9 show the result of that $mset$ scan, which imply $a' = 0.44 \times 50.6 - 0.6 = 21.7 \mu\text{m}$, with an estimated uncertainty of $0.5 \mu\text{m}$ (due to more data points acquired for large A_b). We weight the $E_b=2.1$ and 4.0 GeV results by their inverse square uncertainties to obtain

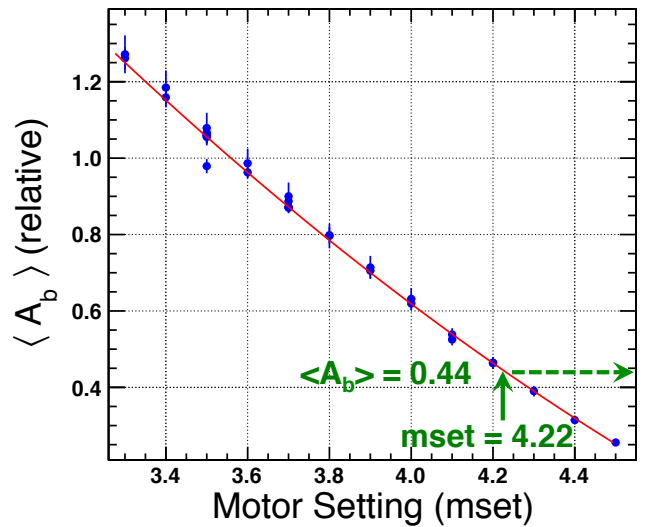


Figure 8: Relative turn-averaged image amplitude $\langle A_b \rangle$ vs. motor setting $mset$ from the xBSM dataset taken at $E_b=2.1 \text{ GeV}$. The overlaid curve represents a third-order polynomial fit to the data points.

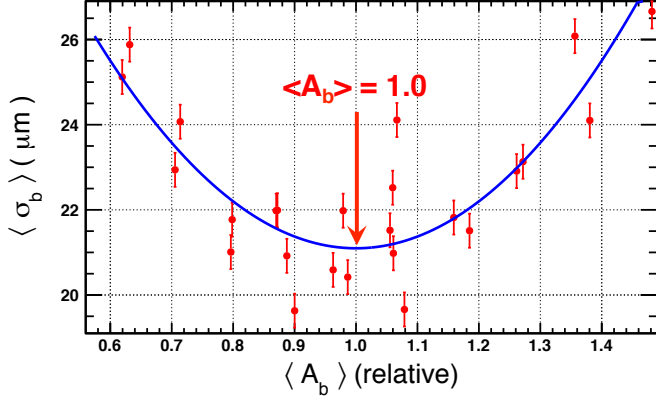


Figure 9: Turn-averaged beam size $\langle \sigma_b \rangle$ vs. relative turn-averaged image amplitude $\langle A_b \rangle$, from the xBSM dataset taken at $E_b=2.1$ GeV.

$a'=22.1 \pm 0.5 \mu\text{m}$. Further analysis of this dataset uses a model with $a'=22 \mu\text{m}$.³

3. Detector spectral response

We define the spectral response of the detector as the (relative) fraction of intensity recorded as pulse height as a function of wavelength. It includes the effect of inactive material in front of the active pixels and the partial absorption as a function of wavelength of the pixels themselves. We measure it using data acquired with various filters in place, wherein each filter masks out some portion of the spectrum different from the other filters. The overall detector spectral response is part of a model described in [1]; the model is adjusted until the predicted integrated intensity on the detector matches the model. We take as our measure of integrated intensity the turn-averaged fitted amplitude per unit beam current, $\langle A_b \rangle$, for a particular run. The turn-by-turn amplitude per unit beam current A_b is the coefficient multiplying a particular best fit, unit-area template that is also fitted for three other free parameters: beam size, beam position, and background constant across the detector. This choice of $\langle A_b \rangle$ is superior to the integrated pulse height because a correct response is still obtained for cases where the beam size is large and the image overflows the detector.

At each of two beam energies, $E_b=2.1$ GeV and 4.0 GeV, data were acquired with no filter in place (NF) and with four or five different filters, shown in Table 2. The thickest filter, Av, was not used at $E_b=2.1$ GeV because it absorbs the entire incident spectrum. Fig. 10 and Table 2 together show the properties of each filter. In particular, Table 2 includes the uncertainty in thickness and its effect upon the uncertainty in energy deposition. This uncertainty was ignored in [1], where the resulting

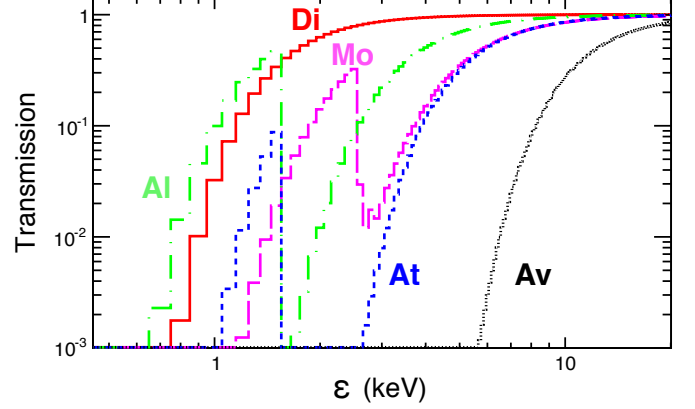


Figure 10: Transmission as a function of x-ray energy ϵ for each of the filters used.

Table 2: Properties of each filter: its name, element, atomic number (A), density (ρ), thickness (T), relative uncertainty in thickness ($\Delta T/T$), relative change in energy deposition per 10% change in thickness ($D_{10}^{E_b}$), for both $E_b=2.1$ and 4.0 GeV.

Name	Element	A	ρ (g/cc)	T (μm)	$\Delta T/T$ (%)	$D_{10}^{2.1}$ (%)	$D_{10}^{4.0}$ (%)
Di	C	12.01	3.515	4.4	10	4.3	0.83
Mo	Mo	95.94	10.28	1.91	3.1	17	5.9
Al	Al	26.98	2.694	7.2	5.0	12	3.1
At	Al	26.98	2.694	22.9	1.4	22	4.1
Av	Al	26.98	2.694	194	0.7	-	12

uncertainty in spectral response was therefore underestimated. Here we account for the effect of that thickness uncertainty in the detector energy deposition from our model, as well as for several effects on the measured values of $\langle A_b \rangle$: uncertainty in current determination and precision, inherent run-to-run variations in the same CESR fill, and fill-to-fill variations due to different horizontal illuminations [1].

The arbitrarily normalized turn-averaged amplitudes for both beam energies and different filters in place are shown in Fig. 11. Note that the filters have much larger relative effects at lower beam energy where the energy absorbed in the filter constitutes a larger fraction of a smaller amount of incident energy.

At this point it is convenient to define two image amplitude ratios, one for data and one for the model. For a particular filter f we define the ratio of the measured turn-averaged amplitude to the corresponding measured no-filter result as

$$R_{data}^f \equiv \frac{\langle A_b \rangle_f}{\langle A_b \rangle_{NF}} \quad (2)$$

and the comparable ratio for the model as

$$R_{model}^f \equiv \frac{A_{b,f}^{model}}{A_{b,NF}^{model}}. \quad (3)$$

We determine the spectral response of the detector by iterating the following process on our model:

³The value of a' extracted from data requires an assumed detector spectral response with this method because diffraction effects vary with both slit size and wavelength. But the detector spectral response is not known *a priori*; it is determined from filter studies in Sect. 3. Hence, the entire analysis of this and subsequent sections was repeated after starting with the response labeled #3 in Fig. 2; the result shown here is from the second iteration, which is $1 \mu\text{m}$ smaller than that of the first iteration.

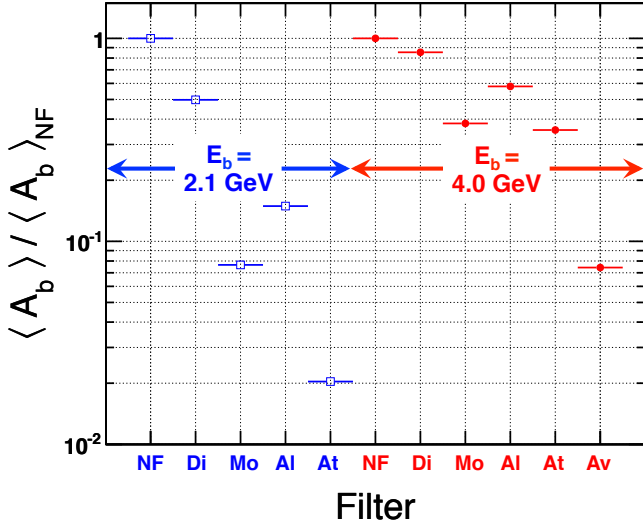


Figure 11: Measured turn-averaged amplitude $\langle A_b \rangle$ using different filters, for $E_b=2.1$ GeV (left, open squares) and 4.0 GeV (right, closed circles). Each set has been normalized to its own arbitrary scale where the no-filter data point has a value of 1.0. Vertical error bars are smaller than the symbols.

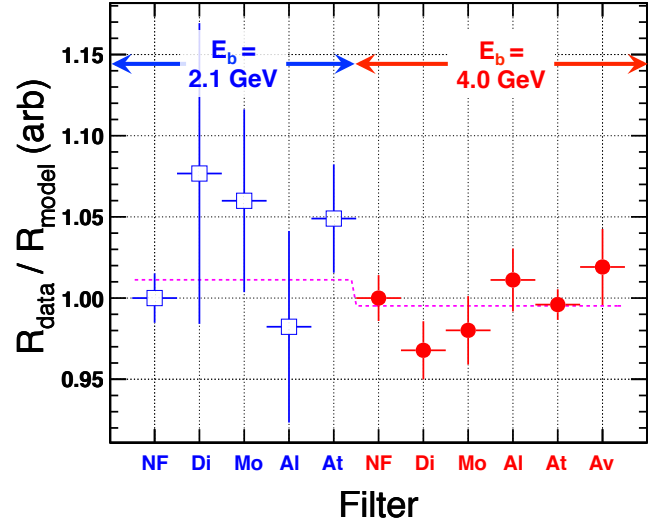


Figure 12: Double ratios $R_{\text{data}}^f / R_{\text{model}}^f$ of measured to predicted image areas for $E_b=2.1$ GeV (left, open squares) and 4.0 GeV (right, closed circles), along with the best-fit values for each energy range shown by the dashed line.

- Adjust the model's spectral response, using a piecewise linear function.
- Run the modified model to obtain the predicted energy deposited into the detector $A_{b,f}^{\text{model}}$ for all the beam energy and filter combinations.
- Calculate the ratio of measured to predicted $R_{\text{data}}^f / R_{\text{model}}^f$, normalizing to the no-filter case separately for $E_b=2.1$ GeV and 4.0 GeV.
- Perform a two-parameter fit to the 11 normalized double ratios of measured to predicted image areas, where the first parameter is the constant value best matching the ratios for $E_b=2.1$ GeV, and the second is the constant value best matching the points for $E_b=4.0$ GeV. These two values may be different from one another, but ideally would be close to unity.
- Calculate the χ^2 for the 9 degrees of freedom of the fit.
- Observing which filter points contribute most to χ^2 , use Fig. 10 to determine where the model's detector response could be altered to improve the fit.

The model-normalized data points and fit for the iterative model optimization are shown in Fig. 12. The fit has $\chi^2 = 8.0$ for 9 degrees of freedom. The error bars on the 2.1 GeV points are dominated by thickness uncertainty due to the filters absorbing a much higher relative fraction of the incident energy than at 4.0 GeV. In order to find a $\sim 1\sigma$ envelope of possible responses, we vary the model in limited ranges of x-ray energy until an increase in χ^2 of 9 units to ~ 18 is obtained. The resulting best-fit response is shown in Fig. 13, along with alternate responses that are each consistent with the data within $\sim 1\sigma$. Figure 14 shows the intensity spectrum after accounting for detector spectral response and filter absorption.

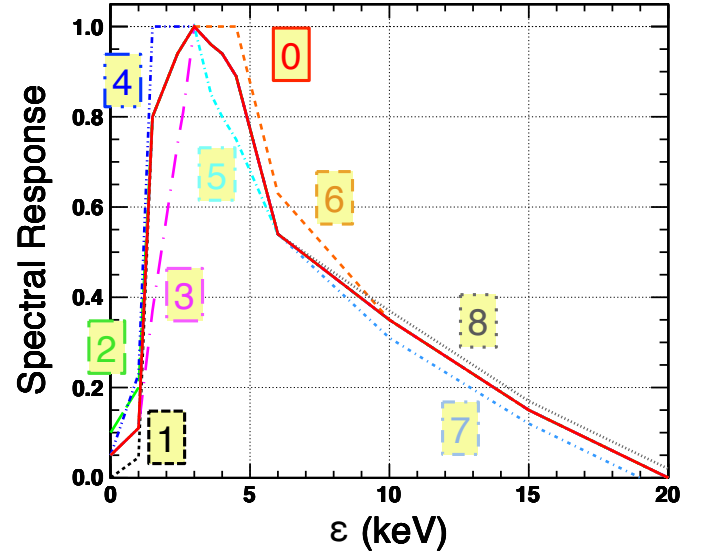


Figure 13: The spectral response of the pixel detector measured from 2.1 GeV and 4.0 GeV data, as described in the text, is shown as the solid line, and labeled by the number 0. Other labeled lines show alternate responses, each of which, by itself, is approximately $\sim 1\sigma$ from nominal. The unseen portions of the lines labeled other than 0 coincide with the nominal response.

4. Beam size studies

In order to evaluate the effectiveness of the spectral response determined in Sect. 3, we can compare the measured vertical beam with different filters in place. The shape of the pinhole prf varies considerably with x-ray energy, as seen in Fig. 15, so inaccuracies in the spectral response will show up as differences in measured beam size when in fact the beam size is the same for all filters.

The data were acquired with each filter at 15 reproducible settings of CESR beam emittance (and thus beam size). If the

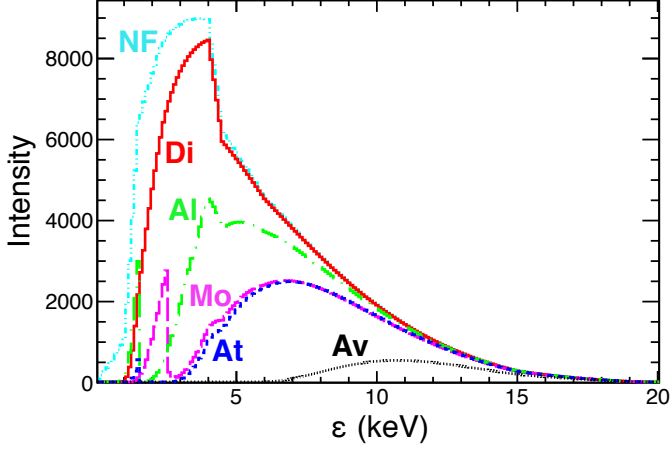


Figure 14: Detected intensity spectrum as a function of x-ray energy for the six filter configurations shown, after accounting for absorption of the filters and the inherent spectral response of the detector.

spectral response is correct, beam sizes measured with data using different filters will all yield the same value at the same emittance setting. The degree of agreement is shown in Fig. 16, where relative differences in measured beam size are seen to be within several percent of one another, with a few outliers above a beam size of $120 \mu\text{m}$. Accuracy for measuring small and moderate beam sizes is at the level of $\pm 4\%$ for all filter configurations.

5. Tilted Detector

The location for a new, dedicated beam size monitor beamline at CESR does not have enough length available for a conventional design: the magnification $M \equiv L'/L$ (see Fig. 1) would be too small, and the detector pitch would become the limiting factor for measurement of small beam sizes. For such a short beamline with small magnification, the image from a small beam through a pinhole optic would become isolated in

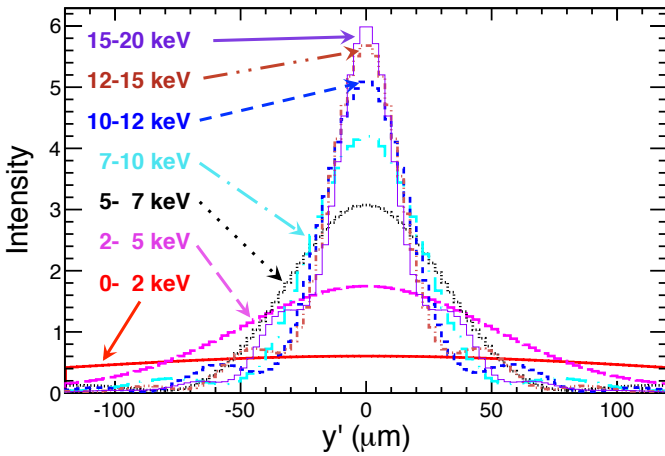


Figure 15: Point response functions (prfs) for a pinhole with a $22 \mu\text{m}$ gap and no filter in place for the x-ray energy ranges shown. All curves are normalized to the same area over the full detector height of 1.6 mm .

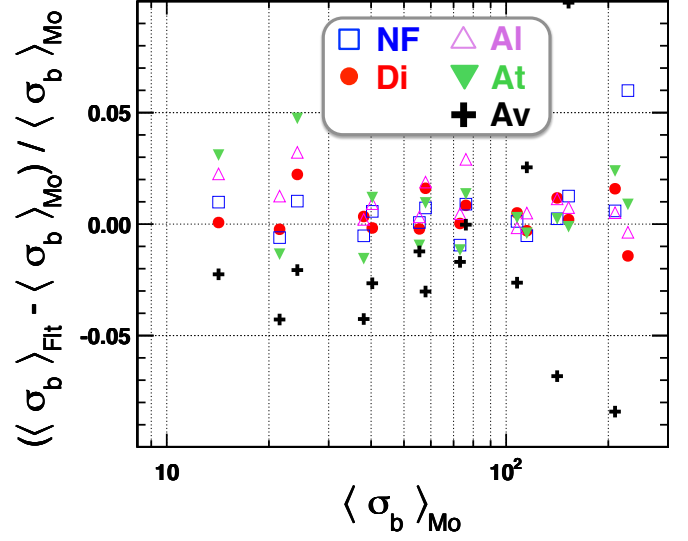


Figure 16: Comparisons of beam sizes obtained with different filters in front of the detector as a function of vertical beam size, using the spectral response of Sect. 3 in creating the prf's applicable to each filter. The vertical axis is the difference between the turn-averaged vertical beam size obtained with a given filter minus that obtained at the same emittance setting with the Mo filter, relative to that obtained with Mo. The horizontal axis is the turn-averaged vertical beam size obtained with the Mo filter for each emittance setting.

just a very few pixels, and resolving power at small beam sizes would become poor. To spread out the image over more pixels without adding length to the beamline, we have elected to tilt the detector forward. A tilt angle of 60° effectively doubles the magnification, although the incident light intensity per pixel is halved. However, tilting the detector also changes its spectral response. On one hand, a tilt increases the effective thickness of the SiN passivation layer, cutting off light at x-ray energies below $\sim 4 \text{ keV}$; on the other, a tilt increases the effective thickness of the active pixel volumes, increasing the absorption at x-ray energies above $\sim 4 \text{ keV}$. In order to explore the net effect of a tilt, we acquired data at $E_b = 2.1$ and 4.0 GeV with the detector tilted vertically at 60° and then remeasured the detector spectral response.

These data were taken using e^- instead of e^+ as in preceding sections. Due to limited beam time available, only two filter configurations (NF and Di) were implemented for the $E_b = 2.1 \text{ GeV}$ data, but the full complement of six sets were acquired for the $E_b = 4.0 \text{ GeV}$ data. The pinhole opening was set at $a' = 49 \mu\text{m}$, the optimal value for $E_b = 2.1 \text{ GeV}$, for both datasets. The ratios of fitted amplitude per unit current are shown in Fig. 17, and the resulting fit to the minimum- χ^2 spectral response in Fig. 18. The minimum- χ^2 spectral response itself appears in Fig. 19, where it is compared to that determined for no tilt.

The spectral response for the 60° -tilted detector differs qualitatively from the no-tilt case in the two expected ways: light absorption is lower (by about 30%) below 4 keV (due to the thicker passivation layer) and higher (by about 100%) above 4 keV . Thus, although tilting the detector spreads incident light over twice the area compared to no-tilt, it recovers absorption

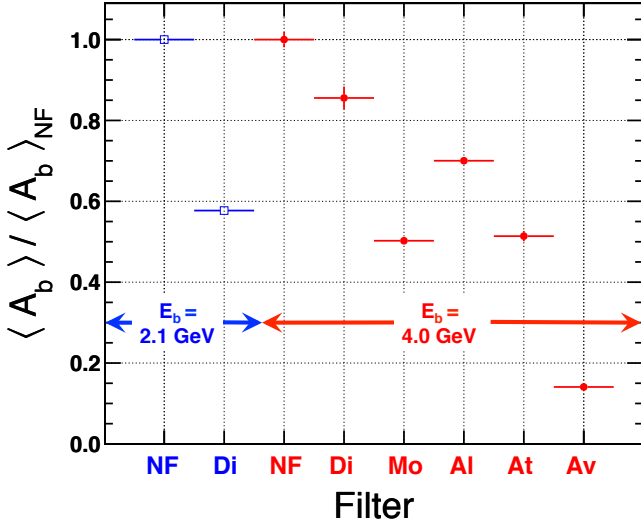


Figure 17: Turn-averaged amplitudes for $E_b=2.1$ GeV (left, open squares) and 4.0 GeV (right, closed circles) for data acquired with a 60° detector tilt. Each set has been normalized to its own arbitrary scale where the no-filter data point has a value of 1.0. Vertical error bars are smaller than the symbols.

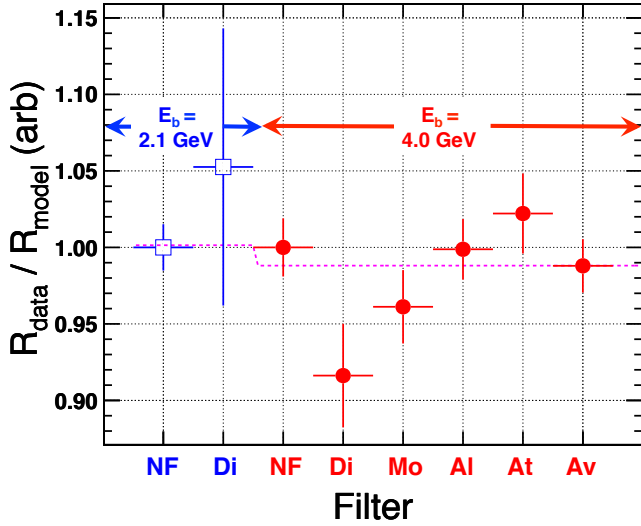


Figure 18: From data acquired with a 60° detector tilt: double ratios R_{data}^f / R_{model}^f of measured to predicted image areas for $E_b=2.1$ GeV (left, open squares) and 4.0 GeV (right, closed circles), along with the best-fit values for each energy range shown by the dashed line.

from x-rays above 4 keV, resulting in a net increase for incident spectra that have a substantial above-4 keV component.

In order to compare beam size capability, three runs were first taken with a particular set of CCSR parameters at $E_b=2.1$ GeV for the detector in the no-tilt configuration. The average value of the beam size was $19.3 \mu\text{m}$. A short time later, three runs with the 60° -tilt were taken for the same beam conditions; these runs had a mean beam size of $19.0 \mu\text{m}$, well within the typical run-to-run variation of beam size measurements. Hence, we have demonstrated that spreading out the x-rays by tilting the detector is a viable method to increase effective magnification

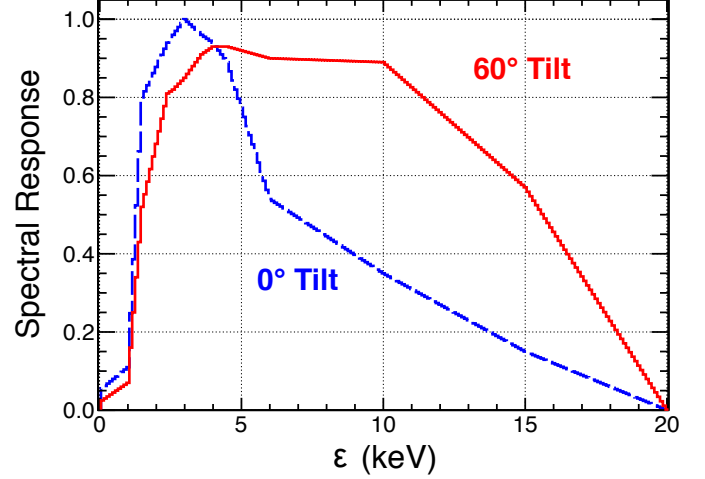


Figure 19: The spectral response of the pixel detector tilted forward by 60° , as measured from 2.1 GeV and 4.0 GeV data, is shown as the solid line. The dashed line corresponds to the spectral response determined for no tilt, as shown in Fig. 13 as the solid line. Relative normalizations for the two curves is arbitrary and not determined by this measurement; however, we expect the two curves to intersect in the 3-6 keV region.

of our pinhole camera as long as a substantial part of the incident spectrum is above 4 keV.

6. Coded aperture

A coded aperture can be useful as an optical element in an x-ray beam-size monitor [1, 2] by improving the resolving power relative to a pinhole. We have found [2] that a carefully designed coded aperture improves performance only at small beam size because at larger beam sizes the multiple peaks in the prf get merged together, whereas at smaller beam size they remain resolved from one another. A coded aperture allows through more light than a pinhole, and uses a larger fraction of the detector by spreading several peaks across it. Downsides of coded apertures can include ineffective patterns for a given incident x-ray energy spectrum, inability to withstand heat loads of intense and/or energetic beams, and heightened sensitivity (relative to a pinhole) to the alignment of the beam with the coded aperture's center.

Here we report briefly on exposure of a coded aperture designated CAHE. The dimensional specifications for the CAHE pattern appear in Fig. 20. The backing is synthetic diamond $350 \mu\text{m}$ thick; the masking is $8 \mu\text{m}$ of gold and $0.1 \mu\text{m}$ of chromium; the manufacturer is Cornes Technology [4]. The CAHE optical element is a prototype being evaluated for use in the x-ray beam size monitor for SuperKEKB.

Fig. 21 shows the predicted resolving power of CAHE and a $22 \mu\text{m}$ pinhole as used in the CCSR positron beam at $E_b=4.0$ GeV. CAHE is expected to yield better performance than this pinhole below about $\sigma_b=15 \mu\text{m}$. Unfortunately, the smallest vertical beam size attained at CCSR for 4.0 GeV positrons is about $\sigma_b=15 \mu\text{m}$, so we can directly compare the pinhole and CAHE only at and above the beam size where the

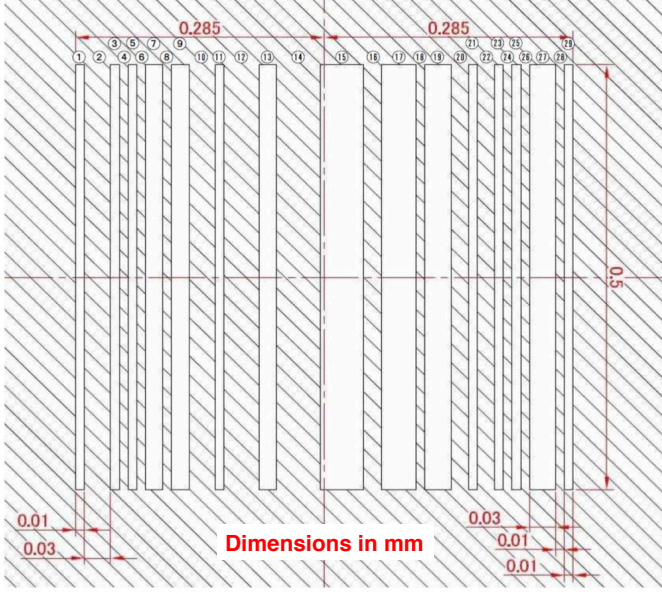


Figure 20: Dimensions of the pattern of the $E_b=4.0$ GeV coded aperture CAHE, which consists of a $350\text{ }\mu\text{m}$ -thick diamond backing with an $8\text{ }\mu\text{m}$ -thick gold (plus $0.1\text{ }\mu\text{m}$ chromium) masking (the masking represented by the hatched area).

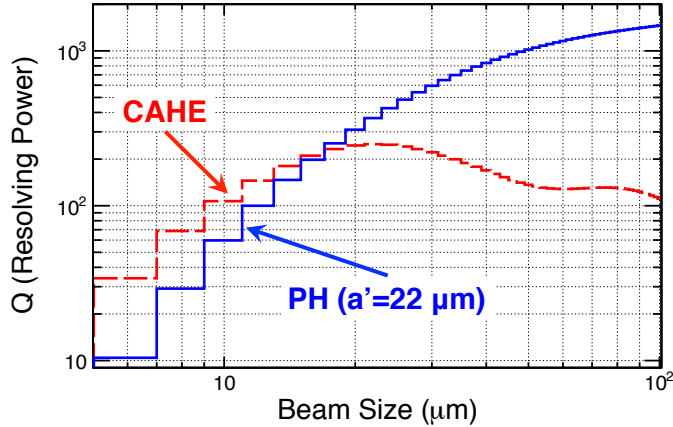


Figure 21: The predicted resolving power Q [1] as a function of beam size at $E_b=4.0$ GeV for a pinhole (PH) with $a'=22\text{ }\mu\text{m}$ (solid line) and the CAHE coded aperture (dashed line).

model predicts that they are equivalent in resolving power. The prf of CAHE is shown in Fig. 22.

Data were acquired at 4.0 GeV with a positron beam on CAHE for the same emittance settings as for the pinhole described previously. We found that beam sizes above about $25\text{ }\mu\text{m}$ were not reproduced well by CAHE and so focus only on the smallest beam size attained, $\sigma_b \approx 15\text{ }\mu\text{m}$. The CAHE images were fit using a fixed detector offset of $d=1\text{ mm}$ (implying that the beam was vertically offset from the center of the CAHE optic by $d/M = 417\text{ }\mu\text{m}$). Figure 23 shows an image of a particular turn at the same beam conditions where the pinhole-determined beam size, averaged over filters, was about $14.3\text{ }\mu\text{m}$. The turn shown yields a beam size of $\sigma_b = 12.4 \pm 1.7\text{ }\mu\text{m}$, and the 1024-turn-averaged beam size is $\langle \sigma_b \rangle = 15.0 \pm 0.1\text{ }\mu\text{m}$, larger than the

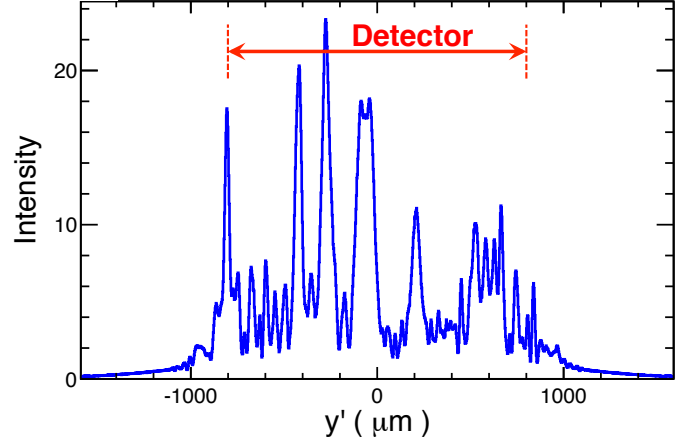


Figure 22: Point response function (prf) for the CAHE coded aperture in the CESR positron beam at 4.0 GeV. The prf overflows our detector; the marked region represents the approximately central exposure detailed in the text.

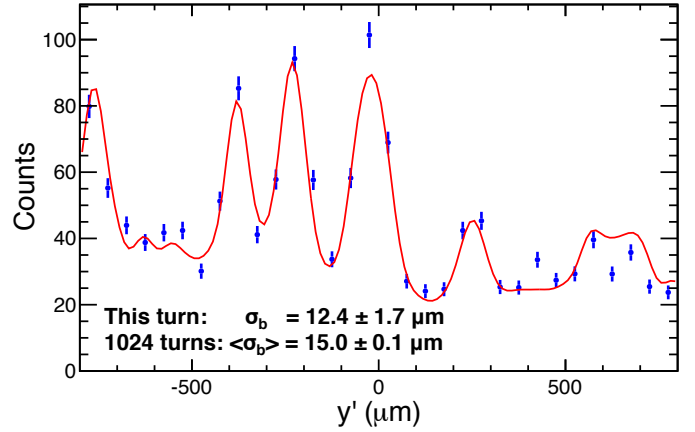


Figure 23: CAHE image from one turn at $E_b=4.0$ GeV overlaid with a fit to beam size, position, and amplitude. The fitted beam size for this turn and the size averaged over all turns in this run are both shown.

pinhole average by $\approx 5\%$.

7. Conclusions

We have extended the characterization of the InGaAs strip detector in the CESR-TA vertical beam size monitor up to an x-ray energy of $\sim 20\text{ keV}$. The spectral response so determined allows determination of the vertical beam size to within $\pm 4\%$ for data acquired using the pinhole optical element at $E_b=4.0\text{ GeV}$. A diamond-backed coded aperture (a prototype optic for beam size monitors at SuperKEKB), was tested for measuring beam size accurately and found to yield accurate ($< 5\%$) results only for small beam sizes ($\sigma_b < 25\text{ }\mu\text{m}$). Measurements taken for a detector pitched forward by 60° showed that we can double the effective magnification of a new, dedicated xBSM beamline for CESR without physically extending the beamline itself.

Acknowledgments

This work would not have been possible without the dedicated and skilled efforts of the CESR Operations Group as well as the support of the Cornell Laboratory for Accelerator-based Sciences and Education (CLASSE) and Cornell High Energy Synchrotron Source (CHESS). This research was supported under the National Science Foundation awards PHY-1002467 and PHY-1416318, and by the NSF and National Institutes of Health/National Institute of General Medical Sciences under NSF award DMR-1332208. It was also supported by the Japan-US Cooperation Program in High Energy Physics.

References

- [1] J. P. Alexander *et al.*, Nucl. Inst. and Methods in Physics Research, A **748** (2014) 96 ([link](#))
- [2] J. P. Alexander *et al.*, Nucl. Inst. and Methods in Physics Research, A **767** (2014) 467 ([link](#))
- [3] Fermionics Opto-Technology, Inc., 4555 Runway St., Simi Valley, CA 93063 USA, www.fermionics.com
- [4] Cornes Technologies K.K., <http://www.cornestech.co.jp>